

# Comparison of Heat Transfer Characteristics of the Hollow-Shaft Oil Cooling System for High Speed Permanent Magnet Synchronous Machines

Runyu Wang, *Student Member, IEEE*, Xinggang Fan, *Member, IEEE*, Dawei Li, *Senior Member, IEEE*, Ronghai Qu, *Fellow, IEEE*, Zirui Liu and Lei Li

State Key Laboratory of Advanced Electromagnetic Engineering and Technology,

School of Electrical and Electronic Engineering,

Huazhong University of Science and Technology, Wuhan 430074, China

**Abstract**—The rotor cooling poses a significant challenge for high speed permanent magnet synchronous machines (PMSMs). This paper presents a recirculating hollow-shaft oil cooling structure. Through the computational fluid dynamics (CFD) method, its convective heat transfer characteristics are studied in depth. Besides, the recirculating hollow-shaft cooling (RHSC) is compared with the direct-through hollow-shaft cooling (DHSC). Based on the CFD analysis, it is found that the convective heat transfer coefficient (CHTC) of the RHSC is higher than that of the DHSC, which can be as high as 58%. Furthermore, the advantage of the RHSC is the most prominent at low rotational speed and small flow rate due to its relatively large oil friction loss at high rotational speed. Moreover, the explanation for the fluctuation of the CHTC before the critical rotational speed, as well as the law of its variation with rotational speed and flow rate, are revealed in this study. The correctness of the simulation analysis is verified by experiments implemented on a rotor setup. In order to summarize the convective heat transfer law of the RHSC better, a dimensionless empirical equation is fitted finally.

**Index Terms**—Convective heat transfer coefficient (CHTC), direct-through hollow-shaft cooling (DHSC), friction loss, oil cooling, permanent magnet synchronous machines (PMSMs), recirculating hollow-shaft cooling (RHSC).

## I. INTRODUCTION

IN recent years, the high power and high speed machines are attracting more and more attentions due to less material consumption and high efficiency. The power density has become one of the most important criteria for lots of applications such as electric vehicles and aircraft generators [1]-[4]. High speed is a key approach to achieve high power density in electrical machines. However, the rotor losses, including bearing loss, air-friction loss and rotor eddy current loss, will increase significantly with higher rotational speed, which leads to a dramatic rise in the rotor loss density [5], [6]. In addition, air can almost be regarded as a thermal insulating material due to its low thermal conductivity, especially at high altitudes, which makes the heat dissipation of the rotor a huge challenge. For permanent magnet electrical machines, high temperature can seriously deteriorate electromagnetic performance and may even cause irreversible demagnetization [7], [8]. Therefore, the rotors of high speed and high power density electrical machines need effective cooling designs.

The high speed rotation of the rotor limits the cooling measures that can be taken, further increases the difficulty of rotor thermal management. Forced air cooling has become the

main method of rotor heat dissipation due to its easy availability, simple cooling system, and low cost [9]-[14]. However, air cooling causes significant vibration noise and air friction loss. Furthermore, as the power density of electrical machines continues to increase, forced air cooling can no longer completely meet the heat dissipation requirements. Since oil or water has higher thermal conductivity and density than air, liquid cooling has emerged as a more effective approach for rotor thermal management [15]. Al-Timimy *et al.* in [16] used oil immersion cooling for the electrical machine as a whole, which greatly shortens the heat transfer path between the heat source and the coolant, thus effectively reducing the rotor temperature and increasing the power density of the electrical machine. However, the rotor's high speed rotation may cause a significant quantity of oil friction loss. The hollow-shaft liquid cooling method is normally employed for rotor thermal management to balance cooling performance, friction loss, and vibration noise. [17], [18].

There are mainly two types of hollow-shaft liquid cooling structures based on flow directions, i.e. recirculating structure and direct-through structure, as shown in Fig. 1. The most crucial feature of hollow-shaft cooling is that the fluid is subjected to centrifugal forces due to the shaft's high speed rotation, resulting in unstable fluid flow. Flow phenomena [19],[20] and pressure losses [21], [22] in a rotating column with axial fluid flow have been investigated. Gai *et al.* in [23], [24] studied the convective heat transfer characteristics of a direct-through hollow-shaft cooling (DHSC), and discussed in detail the effects of rotational speed and flow rate on the convective heat transfer of the system, as well as summarized the dimensionless empirical equations for the DHSC. In order to improve the overall cooling efficiency of the electrical machine further, Lee *et al.* in [25] designed a cooling structure combining housing oil cooling and DHSC together. Lim *et al.* in [26] combines DHSC with oil spray cooling by rotor rotation to impact oil to the winding end, with highly integrated cooling method and high cooling efficiency.

The DHSC is simple in construction, but the seal is more complex, with twice as many dynamic seals and a higher risk of liquid leakage than the recirculating hollow-shaft cooling (RHSC). Gerstler *et al.* in [27] investigated the oil leakage rate of different rotary sealing methods and optimized the geometry of the RHSC to effectively reduce the friction loss and pressure drop of the system. In addition, the inlet and outlet of the RHSC are on the same side, which facilitates an integrated system

design and easy installation of the cooling system at the non-drive end. Accordingly, the RHSC structure is now more extensively employed in industry, for example, in the cooling systems of the Audi e-tron and the Tesla Model S electrical machines [28]. Compared with the DHSC structure, its coolant is introduced via a stationary inner tube and is fed back to the non-driven end due to the function of tail baffle [29], which makes its convective heat transfer characteristics different from the RHSC. Although RHSC structure has currently gained applications, in-depth studies on its fluid flow mechanism and heat transfer characteristics are still lacking. Moreover, there is no detailed comparative analysis of these in the two hollow-shaft structures, which limits the design of such cooling systems and the development of high speed and high power density electrical machines.

To address the previously discussed concerns, the RHSC and the DHSC are compared in this paper. More details and more experimental results are reported as an extension of the work presented in [30]. The structure of the studied electrical machine, the experimental setup of the rotor and the computational fluid dynamics (CFD) models are introduced in Section II. The influence of rotational speed and flow rate on the convective heat transfer of the two hollow-shaft cooling structures and the comprehensive comparison after considering the oil friction loss are discussed in detail in Section III. The experimental validation and analysis of the results of the RHSC will be reported in Section IV. Finally, the conclusions of this research are summarized in Section V.

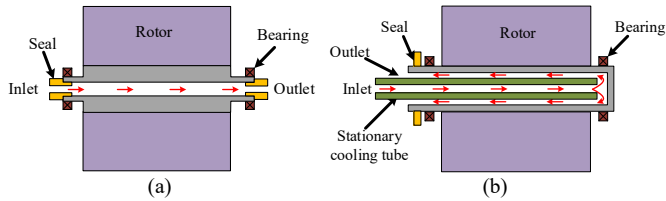


Fig. 1. (a) DHSC structure. (b) RHSC structure.

## II. THERMAL MODEL OF ROTOR SETUP

### A. Studied Machine Structure and Experimental Rotor Setup

In this paper, the hollow-shaft cooling structure for a 130kW aviation fuel pump electrical machine is investigated. The studied machine is an 18-slot 12-pole fractional-slot concentrated-winding (FSCW) permanent magnet electrical machine. Halbach magnet arrays are implemented in the rotor to improve the sine and amplitude of the air-gap magnetic flux density, boost anti-demagnetization capability, and minimize rotor weight. The RHSC is employed due to the large rotor loss of electrical machine with FSCW and the vacuum environment difficult for the rotor to dissipate heat. The split ratio, the magnet pole, and the magnet segment inclined angle are optimized to maximize the power density. The power density of the finally optimized electrical machine power is 5.3kW/kg. The detailed electrical machine parameters are listed in Table I.

The cooling system of the motor is used to dissipate the generated heat as depicted in Fig. 2. There are oil channels in the slot and yoke of the stator, and the coolant is evenly distributed through the oil separator. The rotor is cooled by a

RHSC system. In order to investigate the convective heat transfer characteristics of the hollow-shaft cooling structure, a setup with the same dimensions as the electrical machine rotor as shown in Fig. 3 is fabricated. The heat is generated by injecting current into the heating rod inserted into the outer edge of the rotor, which represents the loss of the permanent magnet. In order to measure average temperature of the shaft wall accurately, holes are drilled on the shaft and rotor spokes, and high-precision temperature sensors (PT100) are inserted. An infrared probe is installed on the front cover to monitor the temperature at the heating rod. Since the heating rods and temperature sensors are installed on the rotor and rotate with it, the wires on them are connected to the outside through a slip ring. The seal is installed between the rotating part and the stationary part to prevent oil leakage. The experimental rotor setup is used as a research object to investigate the convective heat transfer characteristics of the recirculating hollow-shaft.

TABLE I  
MAIN PARAMETERS OF THE PMSM

Parameters	Values
Rated power (kW)	130
Rated torque (Nm)	155
Rated speed (rpm)	8000
Slot/Pole number	18/12
Air-gap radial length (mm)	0.8
Stator outer diameter (mm)	230
Rotor outer diameter (mm)	164.4
Core length (mm)	60
Efficiency (%)	94.5

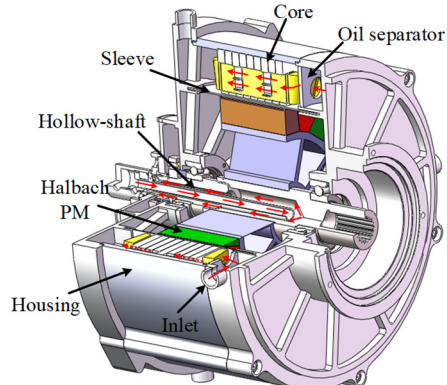


Fig. 2. Studied machine and its cooling system.

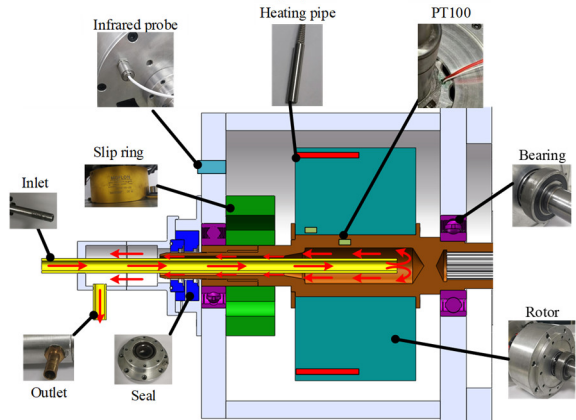


Fig. 3. A section view of the RHSC structure.

The coolant entering the hollow-shaft is a high-temperature

aviation lubricating oil. The relationships between its specific properties and temperature are shown in Table II which are obtained by actual measurements.

TABLE II

THE OIL PROPERTIES CHANGE WITH TEMPERATURE  $T[^\circ\text{C}]$

Properties	Expression
Density [kg/m <sup>3</sup> ]	$\rho = 983.7096 - 0.70054T$
Specific heat [J/kg/°C]	$C_p = 1946.13 + 2.75T$
Thermal conductivity[W/m/°C]	$\lambda_f = 0.15431 - 2.9952E-4T + 4.38737E-7T^2$
Kinematic viscosity [mm <sup>2</sup> /s]	$\nu = 154.41266e^{-0.04562T}$

### B. Governing Equations and Turbulence Model

Since CFD can precisely predict fluid flow and perform conjugate heat transfer analysis, it is used in this paper to investigate the convective heat transfer characteristics of the hollow-shaft. The computational region is spatially discretized into many microelements using the finite volume method at first, then the discrete form of governing equations is solved in each microelement. The governing equations for the CFD model are derived satisfying the mass conservation equation, momentum conservation equation and energy conservation equation. Considering that turbulence is a highly complex three-dimensional non-stationary irregular motion, the flow field variables are generally treated as time-averaged quantities and pulsations to simplify numerical calculation. Therefore, the governing equations are transformed into the form of the following Reynolds Averaged Navier-Stokes (RANS) equations:

$$\frac{\partial \bar{u}_i}{\partial x_i} = 0 \quad (1)$$

$$\frac{\partial(\rho \bar{u}_i)}{\partial t} + \frac{\partial(\rho \bar{u}_i u_j)}{\partial x_j} = -\frac{\partial \bar{p}}{\partial x_i} + \frac{\partial}{\partial x_j} (\mu \frac{\partial \bar{u}_i}{\partial x_j} - \rho \bar{u}'_i \bar{u}'_j) \quad (2)$$

where  $\bar{u}$  is the time-averaged component and  $u'$  is the pulsating component;  $\rho$  is the fluid density;  $t$  is the time;  $p$  is the pressure;  $\mu$  is the fluid dynamic viscosity and  $-\rho \bar{u}'_i \bar{u}'_j$  is the symmetric Reynolds stress tensor with six components.

Following time-homogenization, the equation contains additional terms containing pulsation values that represent the energy transfer due to turbulent pulsations. The presence of these additional terms leads to the problem of non-closure of the basic equations of turbulence. Therefore, the  $k-\varepsilon$  model and the shear stress transport (SST)  $k-\omega$  model both based on the Boussinesq hypothesis are often used to make the system of equations closure [31]. Considering that the CHTC is the focal point of this paper, an appropriate turbulent model which can more correctly account for rotating effects and high shear stresses need to be chosen. The SST turbulence model is chosen since it is more suitable for swirling flows without requiring sublayer damping and includes a nonlinear cubic constitutive relation, which accounts for the anisotropy of turbulence. The  $k-\omega$  model characterizes the dynamics and thermal boundary layer, and the  $k-\varepsilon$  model describes turbulence in the free shear layer, with a blending function transition between the

both. The SST model defines the eddy motion viscosity in order to combine the  $k-\omega$  and  $k-\varepsilon$  models, which can be shown as a unified  $k-\omega$  form:

$$\frac{\partial(\rho k)}{\partial t} + \frac{\partial}{\partial x_j} [\rho u_j k - (\mu + \sigma_k \mu_t) \frac{\partial k}{\partial x_j}] = (\tau_{i,j})_t S_{i,j} - \beta^* \rho w k \quad (3)$$

$$\begin{aligned} \frac{\partial(\rho w)}{\partial t} + \frac{\partial}{\partial x_j} [\rho u_j w - (\mu + \sigma_w \mu_t) \frac{\partial w}{\partial x_j}] = \\ P_w - \beta \rho w^2 + 2(1 - F_1) \frac{\rho \sigma_w}{w} \frac{\partial k}{\partial x_j} \frac{\partial w}{\partial x_j} \end{aligned} \quad (4)$$

where  $\mu_t$  is eddy viscosity;  $S_{i,j}$  is mean-velocity strain-rate tensor;  $k$  is the turbulent kinetic energy;  $w$  is specific dissipation rate;  $\sigma_k$  and  $\sigma_w$  are the Prandtl numbers corresponding to the turbulent kinetic energy and turbulent specific dissipation rate, respectively;  $P_w$  is cross-diffusion term and  $F_1$  is mixed length function.

### C. Mesh and Boundary Conditions

The fluid-solid coupling model of the rotor setup is established, and the three-dimensional mesh is depicted in Fig. 4. Fluent meshing is used to perform the meshing of the fluid-solid coupled domain, and tetrahedral elements are created due to its better adaptability to complex geometries. Solving the laminar boundary layer close to the wall requires very fine meshes to obtain the accurate CHTC. The SST  $k-\omega$  model uses a near-wall turbulence model for the direct solution of the viscous sublayer instead of using the wall function. It requires the dimensionless wall distance  $y^+$  to be less than 1. The value of  $y^+$  can be calculated by (5) and (6).

$$v_* = \sqrt{\frac{\tau_w}{\rho}} \quad (5)$$

$$y^+ = \frac{y \rho v_*}{\mu} \quad (6)$$

where  $v_*$  is friction velocity;  $\tau_w$  is wall shear stress and  $y$  is the normal distance to the wall. The inflations are employed near the wall to capture the velocity and thermal boundary layers. An iterative study was conducted to evaluate whether the solution was grid-independent, which balances both accuracy and speed. The number of mesh elements in the final model is 32 million.

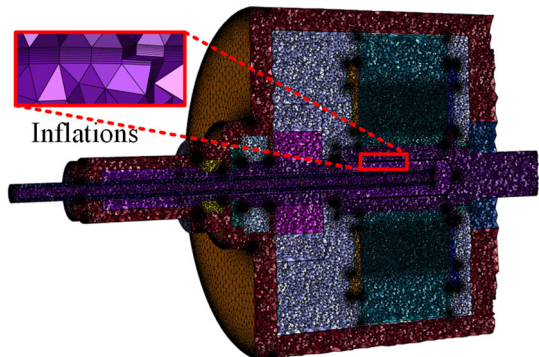


Fig. 4. Mesh of the RHSC structure.

The moving reference frame (MRF) is used to simulate rotation as a key factor influencing convective heat transfer in the hollow-shaft [24]. The volumetric loss is applied to the heating rod and the bearing, and the air friction heat flow loss is applied to the surface of the rotor. Mass-flow-inlet boundary conditions and pressure-outlet boundary conditions are applied at the inlet and outlet, respectively. The housing of the rotor setup is wrapped in heat-insulating wool in order to minimize the heat transfer from the outer walls to the surrounding environment. Therefore, the outer walls of the housing are set as an adiabatic boundary condition. In order to obtain high-accuracy results, a coupled algorithm is used to solve the continuous equation, momentum equation and energy equation at the same time. Outlet temperature and flow rate, the CHTC on the inner wall of the shaft, and other parameters are monitored to assist in judging the convergence of the calculation. It is considered that the solution converges when the residuals of the energy equation are below  $10^{-6}$ , the residuals of the remaining equations are below 0.001, and the monitored physical quantities no longer change with the iterations.

Finally, the simulation is run on a Windows 10 64-bit operating system with a 3.5 GHz CPU and 32 GB RAM, and the solution is completed in about 10 hours.

#### D. Tapered Structure of the RHSC

The tapered structure at the bottom is a major feature of the RHSC compared to the DHSC. Therefore, it is essential to optimize the angle of the tapered structure. The structures with bottom taper angles of  $90^\circ$  and  $180^\circ$  are analyzed while the depth of the shaft is kept consistent. As shown in Fig. 5, the fluid directly impacts the bottom wall with a taper angle of  $180^\circ$  after flowing out of the stationary cooling tube and is subjected to centrifugal forces that generate radial movement. After that, it flows vertically to the junction of the bottom wall and the middle wall, and forms large vortices in the whole bottom area, making the convective heat exchange effect extremely strong. In contrast, the  $90^\circ$  tapered bottom has a certain buffering effect, and the fluid flows down the tapered surface to the annular channel after impact, while forming vortices at the bottom. Fig. 6 shows that the CHTC of the  $90^\circ$  tapered bottom is 8% lower than that of the  $180^\circ$  tapered bottom structure. However, the friction loss is 3.5% higher for  $180^\circ$  tapered structure. More comparison results for different taper angles are shown in Fig. 7. Combined with the actual processing of the drill bit with a certain taper, the final bottom taper angle is determined as  $115^\circ$ .

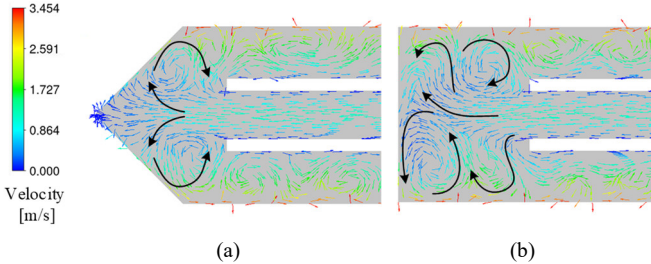


Fig. 5. The velocity vector of the meridian plane of hollow-shaft cooling structure at 1L/min, 3000rpm. (a)  $90^\circ$  tapered structure. (b)  $180^\circ$  tapered structure.

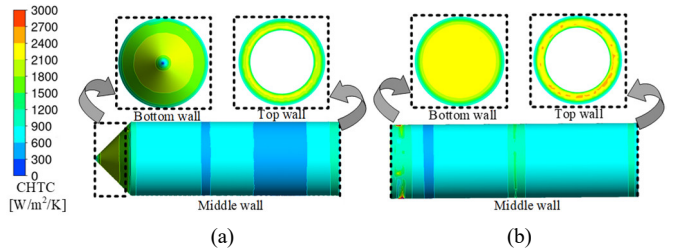


Fig. 6. The CHTC of hollow-shaft cooling structure at 1L/min, 3000rpm. (a)  $90^\circ$  tapered structure. (b)  $180^\circ$  tapered structure.

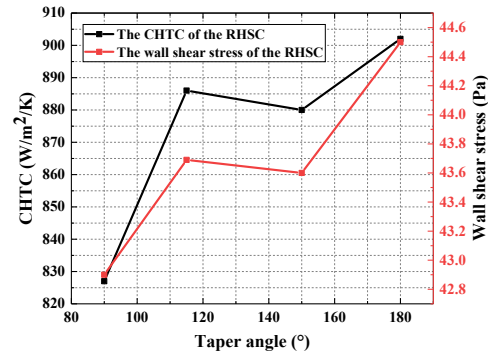


Fig. 7. Comparison of CHTCs and wall shear stresses for the RHSC with different taper angles.

### III. FLUID AND HEAT TRANSFER CHARACTERISTICS OF HOLLOW-SHAFT COOLING

#### A. Characteristics of Fluid Flow in Rotating Shafts

Convection phenomenon occurs when there is a temperature gradient between the solid surface and the flowing fluid. The CHTC is defined to characterize the strength of convective heat transfer, which can be described by Fourier's law using the following equation:

$$h = -\frac{\lambda_f}{\Delta T} \left. \frac{\partial T}{\partial y} \right|_{y=0} \quad (7)$$

Considering convective heat transfer is intimately related to fluid flow, the fluid flow characteristics of the RHSC and the DHSC are first investigated before comparing their convective heat transfer performance. Fig. 8 shows the flow characteristics of the fluid in the hollow-shaft after it has fully developed. As the wall rotation makes the near-wall fluid subject to tangential forces, and at the same time there is a tendency for the fluid within both hollow-shaft structures to flow radially under centrifugal and Coriolis effects, which makes the laminar flow unstable. It is worth noting that the fluid in the RHSC fluctuates significantly in the circumferential direction, forming Taylor vortex with a certain helix angle, which makes the convective heat transfer in the RHSC more superior.

As shown in Fig. 9, the overall average CHTC of the RHSC is higher than that of the DHSC. The oil in the RHSC directly impacts the tapered wall surface, causing a vortex to form. When it flows out of the shaft, it is reflected by the top wall surface to form reverse flows, which makes the turbulence intensity of fluid flow greater and enhances the heat dissipation effect. As a result, the CHTC of the RHSC's bottom and top walls is rather high. Similarly, the local maximum CHTC of the DHSC appears at the bottom and top. However, the area of the

bottom and the top is small, and the heat transfer is limited, hence the convective heat transfer mainly depends on the middle wall.

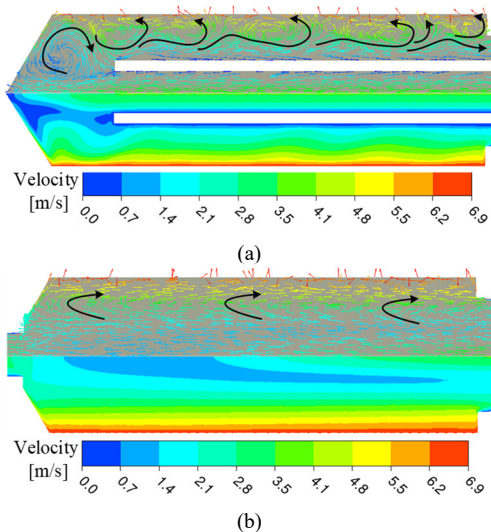


Fig. 8. The velocity cloud diagram and vector diagram of the meridian plane of hollow-shaft cooling structure at 3L/min, 6000rpm. (a) RHSC. (b) DHSC.

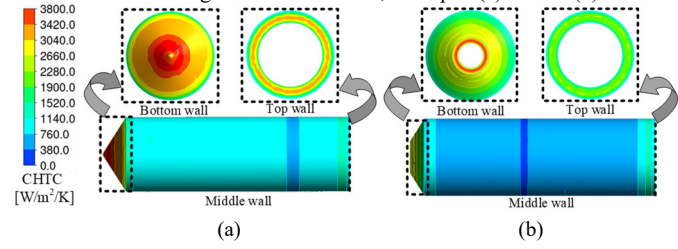


Fig. 9. The CHTC of hollow-shaft cooling structure at 3L/min, 6000rpm. (a) RHSC. (b) DHSC.

### B. Effect of Rotational Speed on the CHTC

To investigate the effect of rotational speed on convective heat transfer in the hollow-shaft, the fluid flow states from low to high rotational speed are analyzed for RHSC and DHSC, respectively, and the results are shown in Fig. 10 and Fig. 11. It is clear that the centrifugal force in the RHSC is weak at 2000rpm, and the flow in the hollow-shaft is relatively stable, with only a vortex developing at the bottom. Taylor vortices begin to form around the middle wall when the speed is increased to 3000rpm. After that, the turbulence of the vortex continues to intensify as the rotational speed increases. Similarly, it can be seen from Fig. 11 that the strength of the fluid vortex of the DHSC is affected by the rotational speed.

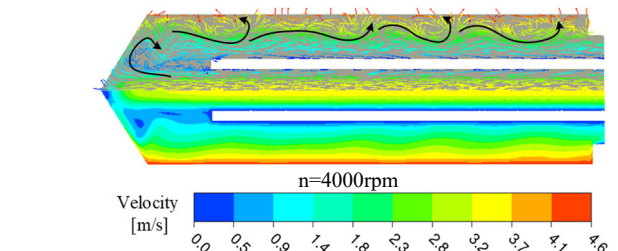
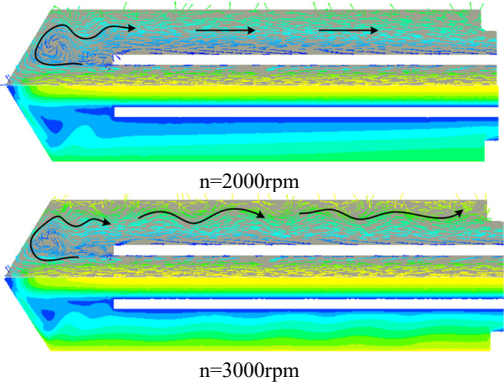


Fig. 10. The velocity cloud diagram and vector diagram of the meridian plane of RHSC structure at different rotational speeds.

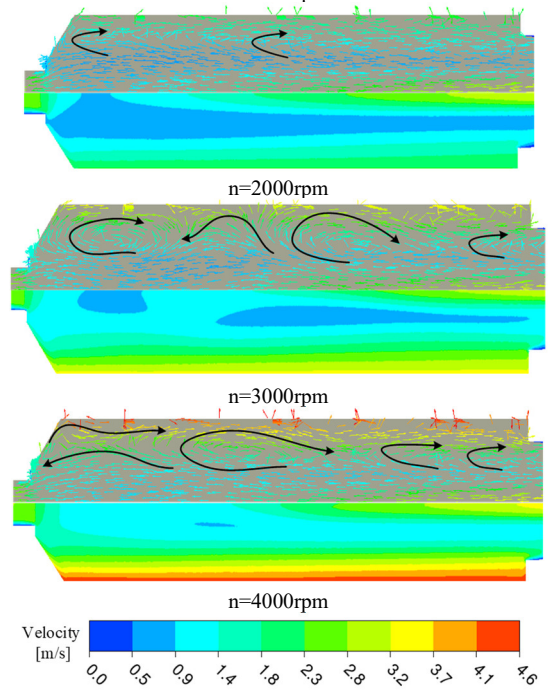


Fig. 11. The velocity cloud diagram and vector diagram of the meridian plane of DHSC structure at different rotational speeds.

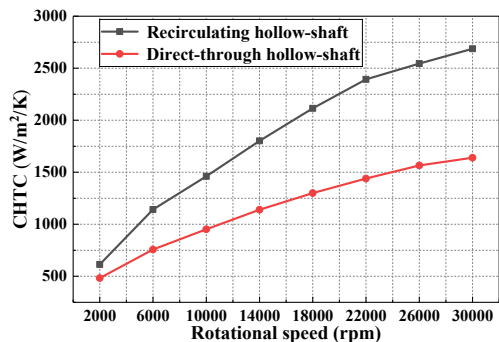


Fig. 12. Variation of the CHTC with rotational speed at 3L/min flow rate.

As illustrated in Fig. 12, the CHTCs of both the RHSC and the DHSC increase with rotational speed under the constant flow rate of 3L/min. The increase in rotational speed strengthens the centrifugal effect and the radial flow tendency of the coolant, thereby enhancing heat exchange and the cooling performance of the system. The bottom surface has the highest CHTC in terms of local CHTC, followed by the top surface. In addition, the CHTC of the RHSC is higher than that of the DHSC, which can be as high as 58%. From the perspective of the growth trend of the CHTC, both the RHSC and DHSC gradually decrease with the increase of rotational speed. The

turbulence of the fluid is practically saturated at high rotational speeds, and the increase in rotational speed is no longer a major influence on convective heat transfer.

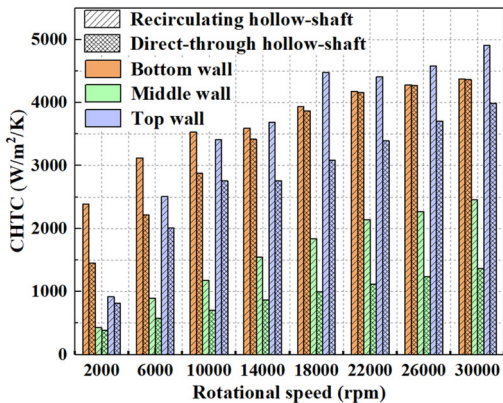


Fig. 13. Variation of the local CHTC with rotational speed at 3L/min flow rate.

### C. Effect of Flow Rate on the CHTC

The flow rate determines the forward movement speed of the heated fluid near the heat exchange wall, making it one of the key factors affecting the CHTC. The overall comparison in Fig. 14 shows that the CHTC of the RHSC is larger than that of the DHSC under different boundary conditions.

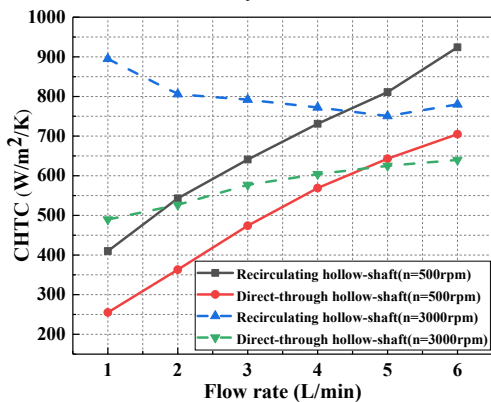


Fig. 14. Comparison of CHTC of two hollow-shafts at the same inlet flow rate.

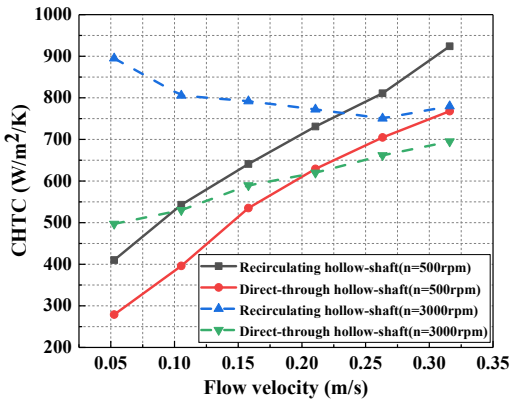


Fig. 15. Comparison of CHTC of two hollow-shafts at the same cross-section flow velocity.

However, it is worth noting that due to the smaller annular cross-section of the RHSC, the average flow velocity of the DHSC section is lower than that of the RHSC section for the same inlet flow rate. In order to provide a fair comparison, it is necessary to ensure that the axial flow velocity is the same in

both hollow-shafts. As shown in Fig. 15, the increase in flow velocity increases the CHTC of the DHSC, but it is still lower than that of the RHSC. It can be seen from Fig. 11 that although the fluid in the DHSC is subject to centrifugal effects and moves radially, the fluid at the center of the shaft flows more smoothly to the outlet due to the lack of a blocking effect at the bottom. In contrast, the fluid in the RHSC forms larger vortices at the bottom due to the blocking effect, after which it flows into a narrow annular cross-section. Therefore, the turbulence of fluid flow in the RHSC is still higher than that of the DHSC.

From the perspective of the growth trend, the CHTC of the two hollow-shaft structures increases with the flow rate at low rotational speed. This is due to the fact that the centrifugal effect weakens at low rotational speeds. It can be seen from Fig. 16 that the fluid is in laminar flow at a speed of 500rpm. At this time, the flow rate becomes the main factor affecting the convective heat transfer. However, the centrifugal and Coriolis effect are strengthened at higher rotational speed, and the Taylor vortex will disappear due to the impact of the increase in flow rate. Therefore, the CHTC of the RHSC gradually decreases as the flow rate increases, and remains almost unchanged after reaching a steady state. Although the CHTC of the DHSC at high rotational speed increases with the flow rate, the growth trend is significantly lower than that at low rotational speed.

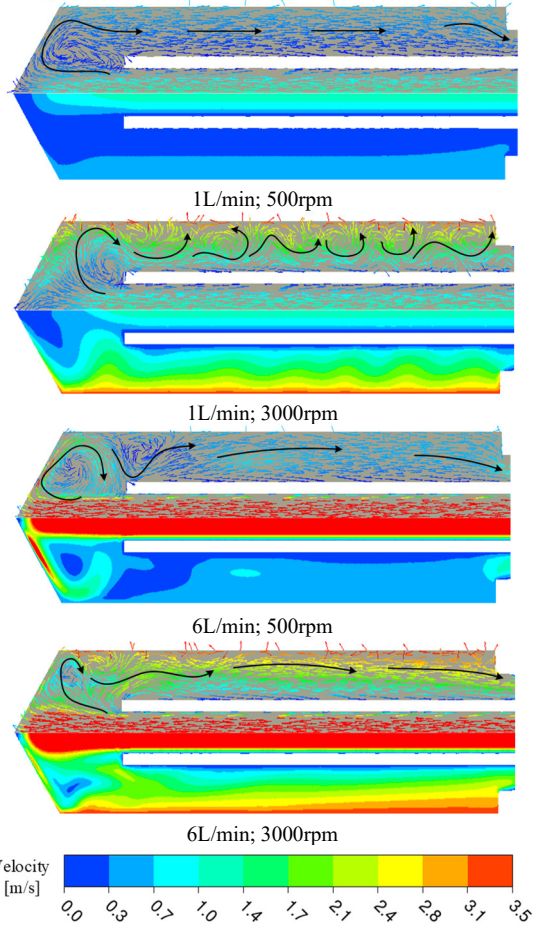


Fig. 16. The velocity cloud diagram and vector diagram of the meridian plane of RHSC structure at different rotational speeds and flow rates.

#### D. Comparison Discussion

According to the aforementioned analysis of the convective heat transfer of the two hollow-shaft cooling structures, the RHSC system outperforms the DHSC system. The RHSC, on the other hand, has a more intense irregular fluid pulsation, as well as a greater friction loss than the DHSC. The oil friction loss of the two hollow-shaft cooling structures at low rotational speed is negligible and can be neglected, as seen in Fig. 17. However, when the rotational speed increases, so does the value of the oil friction loss and the value differential between the two hollow-shafts. The oil friction loss of the RHSC at 30,000rpm is 3.45 times that of the DHSC. Therefore, oil friction loss must be considered when selecting a more suitable hollow-shaft cooling structure.

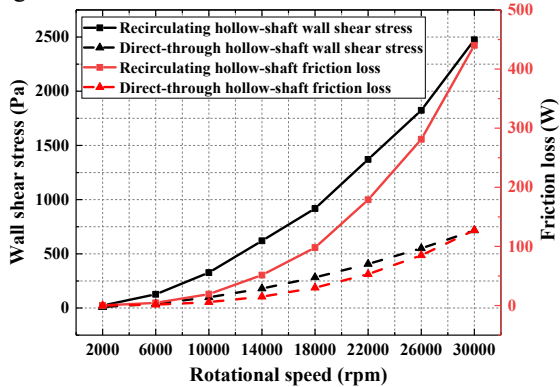


Fig. 17. Variation of the wall shear stress and oil friction loss with rotational speed at 3L/min flow rate.

Take the application of a hollow-shaft cooling system in aviation electrical machines as an example. The electrical machine is located at an altitude of 23km. Due to the thin air, the air friction loss is negligible. The ambient temperature is 120°C, and the temperature of the oil inlet is 93°C. The temperature field distribution characteristics of the two hollow-shaft cooling structures are shown in Fig. 18, and their comparative analysis at different rotational speeds and magnet losses is presented in Fig. 19. It can be found that the advantage of the RHSC becomes increasingly apparent as the rotor loss increases. However, this advantage will gradually disappear at high rotational speed. Under the same rotor loss, the temperature of the rotor with the RHSC first decreases and then increases with the increase of rotational speed. This is attributable to the fact that, although the CHTC is great at high rotational speed, the oil friction loss is large, raising the rotor temperature. As a result, it is necessary to comprehensively consider which hollow-shaft structure to choose according to factors such as rated rotational speed, coolant flow rate, and oil friction loss.

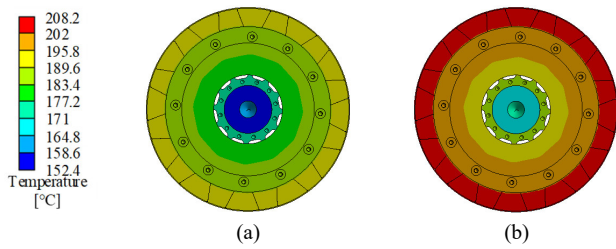


Fig. 18. Temperature fields of two hollow-shaft cooling structures at 3L/min

flow rate, 2000rpm rotational speed, and 350W magnet loss. (a) RHSC. (b) DHSC.

The prominence of the advantages of the RHSC varies with the changes in rotational speed and flow rate, as shown in Fig. 20. The advantage of the RHSC is most outstanding at low rotational speeds and low flow rates, but at high rotational speeds, the RHSC may be inferior to the DHSC due to the existence of oil friction losses. In addition to the advantages of convective heat transfer, the coolant inlet and outlet of the RHSC are on the same side. Only one side requires a dynamic seal, which is beneficial for cooling structure design, system reliability, and reducing the risk of oil leakage. It can be deduced that the RHSC has a greater potential for widespread application.

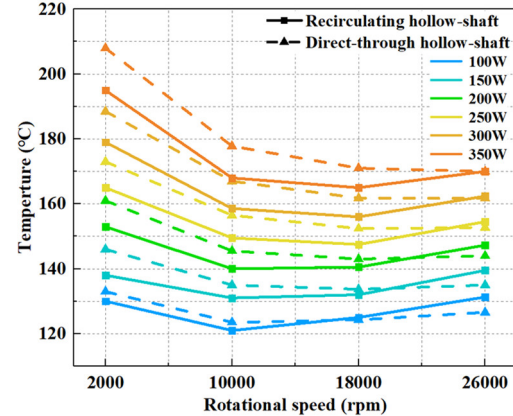


Fig. 19. Variation of the rotor maximum temperature with rotational speed at 3L/min flow rate.

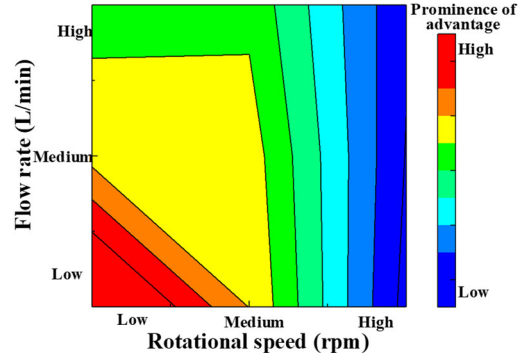


Fig. 20. The prominence of the advantages of the RHSC.

## IV. EXPERIMENTAL VALIDATIONS AND ANALYSIS OF RESULTS

### A. Experimental Setup

The experimental rotor setup of RHSC has been introduced in detail in Section II. Measurement setup and configuration of the rotor experimental platform are shown in Fig. 21. Integrated fuel tank and radiator pump and cool the oil to ensure that the oil temperature is 20°C at the inlet. Temperature sensors (PT100,  $\pm 0.01^\circ\text{C}$ ) and pressure gauges (0.6MPa,  $\pm 3\text{Pa}$ ) are installed at the inlet and outlet to measure the temperature rise and pressure drop of the oil. The prime mover is used to rotate the hollow-shaft with a torque sensor to measure the drag torque. DC power supply to heating pipes to generate heat. In order to reduce the interference of the external environment on the

cooling system of the hollow-shaft, heat-insulating wool is wrapped on the rotor setup housing.

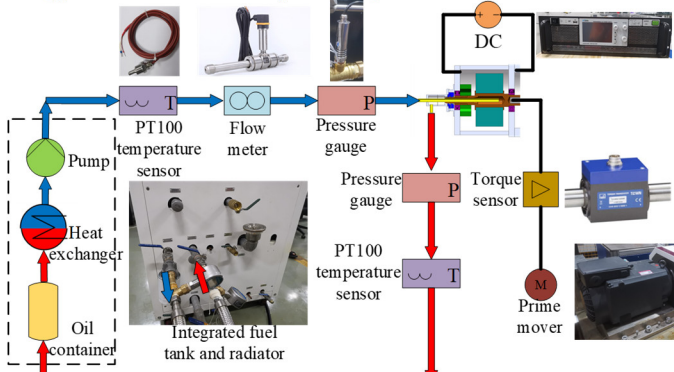


Fig. 21. Test setup and configuration of the rotor experimental platform.

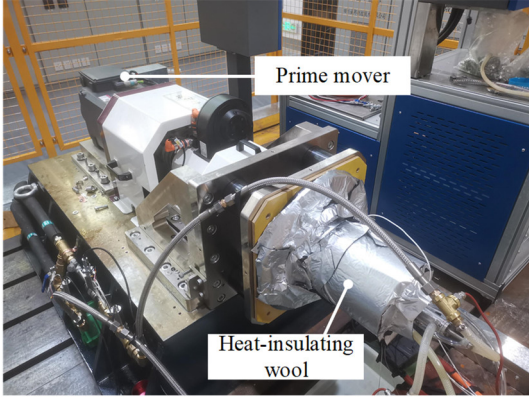


Fig. 22. Overall experiment platform.

### B. The CHTC Calculation

Loss analysis and separation are essential for calculating the CHTC properly. The losses that occur during normal electrical machine operation are classified as electrical joule losses and mechanical losses. Furthermore, mechanical losses are mainly divided into bearing loss, air friction loss, slip ring loss and oil friction loss of hollow-shaft. It can be seen from the analysis in Section III that the oil friction loss at low rotational speed is very small. Therefore, it is only considered at high rotational speed.

Slip ring loss mainly occurs at the brush structure. This part is far away from the hollow-shaft, and its heat dissipation mainly depends on the airflow in the end space and the heat conduction of the endcap, which has almost no effect on the cooling of the hollow-shaft.

Bearing loss is caused by the friction between the balls and the bearing ring when the rotor rotates, and its heat transfer mechanism is more complicated. Bearing loss is closely related to lubricating oil viscosity, rotational speed and rotor mass. For small and medium power electrical machines, the bearing loss can be calculated as follows:

$$P_{bearing} = 0.03k_{fb}(m_r + m_{sh})\frac{W}{\pi} \quad (8)$$

where  $k_{fb}$  is the bearing loss coefficient, for small and medium-sized bearings, the range is between  $1\sim 3\text{m}^2/\text{s}^2$ .  $m_r$  and  $m_{sh}$  are the masses of the electrical machine rotor and shaft, respectively.

The rotating electromagnetic torque generates a shear force between the rotor wall and the internal air, which hinders the movement of the rotor and generates air friction loss. The air friction loss is related to the roughness of the rotor wall, the rotational speed, the geometric model of the rotor, the velocity distribution in the airgap, and the physical properties of the air. The following empirical equation calculations are commonly used:

$$P_{airgap} = k_1 C_f \rho \pi w^3 r_1^4 l \quad (9)$$

$$P_{endsurface} = 0.5 C_f \rho W^3 (r_1^5 - r_2^5) \quad (10)$$

where  $P_{airgap}$  and  $P_{endsurface}$  are the air friction loss on the air gap side surface and the front and rear end surfaces of the rotor, respectively;  $k_1$  is the roughness coefficient, with a value range of  $1\sim 2.5$ , where 1 means that the wall surface is completely smooth.  $r_1$  and  $r_2$  are the outer radius of the rotor and shaft.  $l$  is the axial length of the rotor.  $C_f$  is the coefficient of friction, which is related to the shear stress on the rotor surface and can be calculated by the empirical equation in [1].

Four experimental steps are taken to separate and calculate the power loss extracted by the cooling of the hollow-shaft:

1) Let the shaft without a slip ring structure rotate without passing the oil and turn off the DC power supply: the main losses in this case are bearing loss and air friction loss on the outer surface of the rotor;

2) Install the slip ring structure and repeat the previous step: in this case, the slip ring loss can be separated;

3) Apply oil to the shaft and rotate it while turning off the DC power: in this case, oil friction loss can be separated. Based on the data measured by the torque sensor, the total mechanical loss can be calculated. There are two main ways to dissipate the heat generated by mechanical loss: one is to use the conduction effect to transfer the heat to the shaft and dissipate it through the hollow-shaft cooling system, and the other is to remove the heat by convection caused by the airflow inside the electrical machine. Among them, the heat dissipated by the hollow-shaft cooling system is defined as:

$$P_{DCoff} = q_m * C_p * (T_{out} - T_{in}) \quad (11)$$

where  $q_m$  is the mass flow;  $T_{in}$ ,  $T_{out}$  are the inlet and outlet oil temperatures that can be measured with PT100 sensor.

4) Apply oil to the shaft and rotate it while turning on the DC power: the input electric power  $P_e$  will be converted into a heat source by the heating rod and applied to the rotor. Most of the electrical power will be dissipated through the hollow-shaft cooling system. In order to accurately separate this part of the loss, equation (11) is used to calculate the power  $P_{DCon}$  be removed by the oil at this time. Finally, the average CHTC of the hollow-shaft can be calculated using the following equation:

$$h = \frac{(P_{DCon} - P_{DCoff}) / S}{T_{wall} - T_f} \quad (12)$$

where  $S$  and  $T_{wall}$  are the area and average temperature of the convective heat transfer surface of the hollow-shaft, respectively;  $T_f$  is the average temperature of inlet and outlet oil.

Due to the limitation of the experimental platform and safety reasons, the maximum rotational speed of the experimental test is 5000rpm. The temperature can be considered stable when the monitored temperature reading

remains constant for several consecutive minutes. Owing to the external heat-insulating wool wrap, the rotor setup takes only about 20 minutes to reach steady state.

### C. Results and Discussion

#### 1) Analysis of the Impact of Rotational Speed and Mass Flow

The rotational speed of the shaft is increased from 0rpm to 5000rpm. At the same time, the flow rate has changed from 1L/min to 4L/min. Equation (12) is used to calculate the experiment's CHTC, which is then compared to the simulation results, as shown in Fig. 23. It can be seen that the experimentally measured CHTC is on the low side. This might be attributed to a little shift in the position of the temperature sensor. Existing experimental results show that the maximum error is 30%, the minimum error is 13%, and the overall average error is within 20%. The change trend reflected by the experimental measurement data is consistent with the simulation result, which further verifies the correctness of the previous simulation analysis.

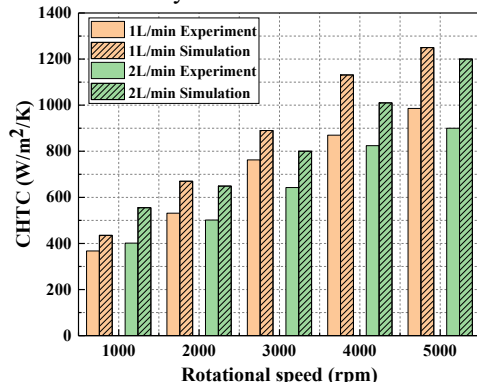


Fig. 23. Comparison of experimental and simulated results with rotational speed from 1000 to 5000rpm.

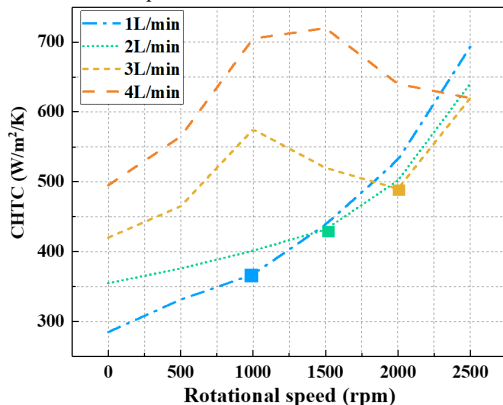


Fig. 24. Variation of the experimentally measured CHTC with rotational speed and flow rate.

It is noteworthy that the trend of the CHTC with rotational speed shows diversity at low rotational speeds. The CHTC at flow rates of 1L/min and 2L/min follows the same trend as rotational speed, increasing slowly at first and then sharply, as shown in Fig. 24. It can be seen from the analysis in Section III that the centrifugal effect at low rotational speed is weak, and the fluid is in laminar flow. At this time, the speed has little effect on the CHTC, and therefore the growth trend is relatively slow. When the rotational speed increases to the critical rotational speed, Taylor vortex is formed in the hollow-shaft,

thus the CHTC increases sharply as the rotational speed increases. In Fig. 24, square labels are used to denote critical rotational speed points. It can be seen that the larger the flow rate, the higher the critical rotational speed. This is caused by the stronger axial impact of the high flow on the Taylor vortex and the greater centrifugal force required to form the Taylor vortex.

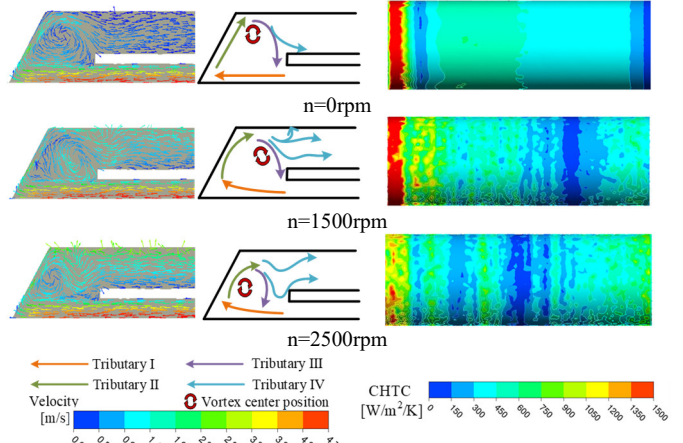


Fig. 25. The velocity vector and the CHTC of RHSC structure at 4L/min flow rate.

When the flow rate is increased to 3L/min and 4L/min, the CHTC does not grow in a monotonic ascending trend before reaching the critical rotational speed, but increases first and then decreases. The velocity vector at 0rpm, 1500rpm and 2000 rpm when the flow rate is 4L/min is depicted in Fig. 25. The vortex in the bottom area is divided into four tributaries in order to clearly explain the changes in the growth trend. When the shaft is stationary, the fluid is no longer affected by the centrifugal force, and the Tributary II impinges the middle wall along the bottom surface of the cone. After encountering the obstruction of the drainage tube, the Tributary III and the Tributary IV are formed. In this case, the center of the vortex is located near the junction of the tapered bottom wall and the middle wall. It can be seen from Fig. 25 that the local CHTC in the bottom area of the middle wall is the highest. When the rotational speed rises to 1500rpm, Tributary I and Tributary II tend to move radially due to the increase of centrifugal force, Tributary IV fluctuates slightly and impacts the middle wall again. The fluid turbulence in the bottom area of the middle wall is further aggravated, and the local CHTC is higher than the case where the rotational speed is 0rpm. Therefore, as the rotational speed increases, the overall average CHTC shows an increasing trend. When the rotational speed is 2500rpm, due to the excessive centrifugal force, the center of the vortex is far away from the middle wall of the shaft, causing the convective heat transfer effect in the bottom area to weaken. However, the rotational speed at this time has not reached the critical rotational speed that can form Taylor vortex. Therefore, when the rotational speed rises from 1500 rpm to the critical rotational speed, the overall CHTC gradually decreases.

The trend of the CHTC before the critical rotational speed can be understood as a “fluctuation”. There is no “fluctuation” phenomenon when the flow rate is low. As the flow rate increases, the magnitude of the “fluctuation” and the

corresponding rotational speed range increase.

## 2) Influence of Inlet Temperature

As can be seen from Table II, among these physical properties, viscosity is the most sensitive to temperature. When the temperature rises from room temperature, the viscosity decreases exponentially. Change the inlet temperature and measure the CHTC at different rotational speeds. The result is shown in Fig. 26. The increase in inlet temperature increases the CHTC by about 15%, which is due to the decrease in viscosity that enhances the effect of convective heat transfer.

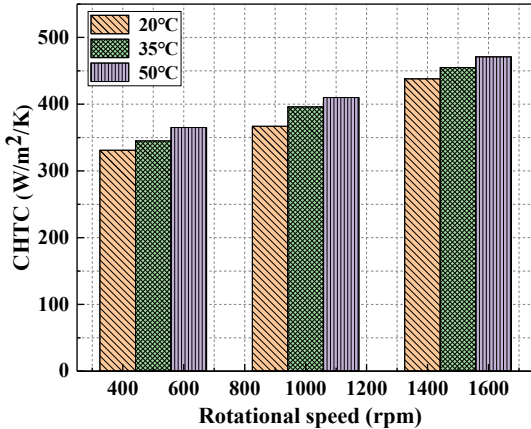


Fig. 26. The CHTC at different inlet temperatures.

## 3) Dimensionless Analysis

Convective heat transfer is related to the physical properties of the fluid, the state of motion, and the geometric structure of the heat exchange surface. In order to better analyze and summarize the convective heat transfer phenomenon of fluids, Reynolds number, Nusselt number and Prandtl number are defined:

$$Re_r = \rho * V_r * D_r / \mu \quad (13)$$

$$Re_a = \rho * V_a * D_r / \mu \quad (14)$$

$$Nu = D_r * h / \lambda_f \quad (15)$$

$$Pr = C_p * \mu / \lambda_f \quad (16)$$

where  $Re_a$  and  $Re_r$  are the axial Reynolds Number and rotational Reynolds Number;  $D_r$  is the hydraulic diameter;  $V_a$  and  $V_r$  are the axial and tangential velocities.

Through dimensionless analysis and fitting of all experimental data, the following empirical equation can be obtained:

$$Nu = A * Re_r^B * Pr^{0.4} + C * Re_a^D * Pr^{0.4} \quad (17)$$

where  $A$  is 0.0122,  $B$  is 0.744,  $C$  is 0.8115,  $D$  is 0.132. The resulting equation is valid when  $Re_r$  varies from 0 to 633 and  $Re_a$  varies from 5.7 to 23.1.

## V. CONCLUSION

In this paper, the convective heat transfer characteristics of two hollow-shaft cooling systems are analyzed. The results show that the CHTCs of two hollow-shaft structures increase with rotational speed and eventually tend to saturate. The effect of flow rate on convective heat transfer shows diversity, and the trend of the CHTC with flow rate is related to the critical rotational speed. A comprehensive comparison of the two hollow-shafts, taking into account oil frictional loss, shows that

the advantages of the RHSC system are more prominent at low rotational speeds and low flow rates. Furthermore, the fluctuation of convective heat transfer characteristics of the RHSC in the low rotational speed range is investigated in this paper. The CHTC tends to increase and then decrease with increasing rotational speed until the rotational speed reaches the critical rotational speed. The amplitude of the fluctuation and the corresponding speed range increase with the flow rate. The trend of the experimental results is consistent with the simulation, which verifies the correctness of the simulation analysis. The dimensionless empirical equations that have been fitted can be used to optimize the RHSC system. The heat dissipation performance of the RHSC structure in real electrical machines and the experimental structure at higher rotational speeds will be reported in the future.

## REFERENCES

- [1] X. Fan, B. Zhang, R. Qu, D. Li, J. Li and Y. Huo, "Comparative thermal analysis of IPMSMs with integral-slot distributed-winding (ISDW) and fractional-slot concentrated-winding (FSCW) for electric vehicle application," *IEEE Trans. Ind. Appl.*, vol. 55, no. 4, pp. 3577-3588, July/Aug. 2019.
- [2] X. Fan, D. Li, R. Qu, C. Wang and H. Fang, "Water cold plates for efficient cooling: Verified on a permanent-magnet machine with concentrated winding," *IEEE Trans. Ind. Electron.*, vol. 67, no. 7, pp. 5325-5336, July 2020.
- [3] K. T. Chau, C. C. Chan and C. Liu, "Overview of permanent-magnet brushless drives for electric and hybrid electric vehicles," *IEEE Trans. Ind. Electron.*, vol. 55, no. 6, pp. 2246-2257, June 2008.
- [4] V. Madonna, P. Giangrande and M. Galea, "Electrical power generation in aircraft: Review, challenges, and opportunities," *IEEE Trans. Transp. Electricif.*, vol. 4, no. 3, pp. 646-659, Sept. 2018.
- [5] T. Han, Y. Wang and J. -X. Shen, "Analysis and experiment method of influence of retaining sleeve structures and materials on rotor eddy current loss in high-speed PM motors," *IEEE Trans. Ind. Appl.*, vol. 56, no. 5, pp. 4889-4895, Sept/Oct. 2020.
- [6] N. Chiodetto, N. Bianchi and L. Alberti, "Improved analytical estimation of rotor losses in high-speed surface-mounted PM synchronous machines," *IEEE Trans. Ind. Appl.*, vol. 53, no. 4, pp. 3548-3556, July/Aug. 2017.
- [7] S. Ruoho, J. Kolehmainen, J. Ikaheimo and A. Arkkio, "Interdependence of demagnetization, loading, and temperature rise in a permanent-magnet synchronous motor," *IEEE Trans. Magn.*, vol. 46, no. 3, pp. 949-953, March 2010.
- [8] A. Lindner, K. Litvinova, G. Popov and I. Hahn, "Measurement of rare earth magnets at high temperatures," in *Proc. Int. Symp. Power Electron., Electr. Drives, Autom. Motion*, Anacapri, 2016, pp. 213-220.
- [9] A. S. Bornschlegel, J. Pelle, S. Harmand, A. Fasquelle and J. Corriou, "Thermal optimization of a high-power salient-pole electrical machine," *IEEE Trans. Ind. Electron.*, vol. 60, no. 5, pp. 1734-1746, May 2013.
- [10] T. D. Kefalas and A. G. Kladas, "Thermal investigation of permanent-magnet synchronous motor for aerospace applications," *IEEE Trans. Ind. Electron.*, vol. 61, no. 8, pp. 4404-4411, Aug. 2014.
- [11] P. Asef, R. B. Perpina and M. R. Barzegaran, "An innovative natural air-cooling system technique for temperature-rise suppression on the permanent magnet synchronous machines," *Electr. Power Syst. Res.*, vol. 154, pp. 174-181, 2018.
- [12] A. Nollau and D. Gerling, "A new cooling approach for traction motors in hybrid drives," in *Proc. Int. Elect. Mach. Drives Conf.*, May 12-15, 2013, pp. 456-461.
- [13] S. Noda, S. Mizuno, T. Koyama and S. Shiraishi, "Development of a totally enclosed fan cooled traction motor," in *Proc. IEEE Energy Convers. Congr. Expo.*, 2010, pp. 272-277.
- [14] A. S. Lapkov and A. M. Litvinenko, "Analysis of efficiency of cooling system of hollow-shaft automotive alternator," *Russ. Electr. Engin.*, vol. 81, no. 10, pp. 554-558, Oct. 2010.

- [15] F. Guo and C. Zhang, "Oil-cooling method of the permanent magnet synchronous motor for electric vehicle," *Energies*, vol. 12, no. 15, pp. 1-11, 2019.
- [16] A. Al-Timimy, P. Giangrande, M. Degano, Z. Xu, M. Galea, C. Gerada, G. L. Calzo, H. Zhang and L. Xia, "Design and losses analysis of a high power density machine for flooded pump applications," *IEEE Trans. Ind. Appl.*, vol. 54, no. 4, pp. 3260-3270, July/Aug. 2018.
- [17] M. Kimiaeigui, J. D. Widmer, R. Long, Y. Gao, J. Goss, R. Martin, T. Lisle, J. M. S. Vizan, A. Michaelides and B. Mecrow, "High-performance low-cost electric motor for electric vehicles using ferrite magnets," *IEEE Trans. Ind. Electron.*, vol. 63, no. 1, pp. 113-122, Jan. 2016.
- [18] D. J. B. Smith, "High speed high power electrical machines," Ph.D. dissertation, Dep. Mech. Eng., Newcastle Univ., Newcastle, UK, 2014.
- [19] S. Seghir-Ouali, D. Saury, S. Harmand, O. Phillipart, and D. Laloy, "Convective heat transfer inside a rotating cylinder with an axial air flow," *Int. J. Thermal Sci.*, vol. 45, no. 12, pp. 1166-1178, 2006.
- [20] G. Reich, B. Weigand, and H. Beer, "Fluid flow and heat transfer in an axially rotating pipe-II. Effect of rotation on laminar pipe flow," *Heat Mass Transfer*, vol. 32, no. 3, pp. 563-574, 1989.
- [21] A. White, "Flow of a fluid in an axially rotating pipe," *Journal Mechanical Engineering Science*, vol. 6, no. 1, 1964.
- [22] Y. Gai, Y. C. Chong, H. Adam, J. Goss and M. Popescu, "Power losses and thermal analysis of a hollow-shaft rotor cooling system," in *Proc. 22nd Int. Conf. Electr. Mach. Syst.*, 2019, pp. 1-6.
- [23] Y. Gai, J. D. Widmer, A. Steven, Y. C. Chong, M. Kimiaeigui, J. Goss and M. Popescu, "Numerical and experimental calculation of CHTC in an oil-based shaft cooling system for a high-speed high-power PMSM," *IEEE Trans. Ind. Electron.*, vol. 67, no. 6, pp. 4371-4380, June 2020.
- [24] Y. Gai, Y. C. Chong, H. Adam, X. Deng, M. Popescu and J. Goss, "Thermal analysis of an oil-cooled shaft for a 30 000 r/min automotive traction motor," *IEEE Trans. Ind. Appl.*, vol. 56, no. 6, pp. 6053-6061, Nov./Dec. 2020.
- [25] K. H. Lee, H. R. Cha and Y. B. Kim, "Development of an interior permanent magnet motor through rotor cooling for electric vehicles," *Applied Thermal Engineering*, vol. 95, pp. 348-356, 2016.
- [26] D. H. Lim and S. C. Kim, "Thermal performance of oil spray cooling system for in-wheel motor in electric vehicles," *Applied Thermal Engineering*, vol. 63, no. 2, pp. 577-587, 2014.
- [27] W. Gerstler, E. Ruggiero, F. Ghasripor, A. El-Refaie and J. Alexander, "A liquid-cooled rotor for high density electric machines," in *Proc. 47th AIAA/ASME/SAE/ASEE Joint Propuls. Conf. Exhib.*, Jul. 2011, p. 5560.
- [28] P. Zhou, N. R. Kalayjian, G. D. Cutler and P. K. Augenbergs, "Liquid cooled rotor assembly," U.S. Patent 20090121563 A1, May. 14, 2009.
- [29] A. M. EL-Refaie, J. P. Alexander, S. Galioito, P. B. Reddy, K. Huh, P. D. Bock and X. Shen, "Advanced high-power-density interior permanent magnet motor for traction applications," *IEEE Trans. Ind. Appl.*, vol. 50, no. 5, pp. 3235-3248, Sept./Oct. 2014.
- [30] R. Wang, X. Fan, D. Li and R. Qu, "Comparison of two hollow-shaft liquid cooling methods for high speed permanent magnet synchronous machines," in *Proc. IEEE Energy Convers. Congr. Expo.*, 2020, pp. 3511-3517.
- [31] X. Fan, R. Qu, J. Li, D. Li, B. Zhang and C. Wang, "Ventilation and Thermal Improvement of Radial Forced Air-Cooled FSCW Permanent Magnet Synchronous Wind Generators," *IEEE Trans. Ind. Appl.*, vol. 53, no. 4, pp. 3447-3456, July/Aug. 2017.



**Runyu Wang** was born in Anhui, China. He received the B.Eng. degree in electrical engineering and automation from Anhui University, Hefei, China, in 2019. He is currently working toward the Ph.D. degree in Huazhong University of Science and Technology, Wuhan, China. His research interests include electromagnetic and cooling design of high power density permanent magnet machines.



**Xinggang Fan** (S'16-M'21) was born in Hubei, China. He received the B.Eng. degree in energy engineering and Ph.D. degree in electrical engineering from Huazhong University of Science and Technology, Wuhan, China, in 2014 and 2019, respectively. He is currently a Postdoctoral Fellow with this university. His research interests include electromagnetic-thermal design and analysis of permanent magnet machines, especially those working in the high power density occasions.



**Dawei Li** (S'12-M'15-SM'21) was born in China. He received the B.Eng. degrees in electrical engineering from Harbin Institute of Technology, Harbin, China, in 2010, and Ph.D. degree in electrical engineering, from Huazhong University of Science and Technology, Wuhan, China, in 2015. His research interests include design and analysis of novel permanent-magnet brushless machines.



**Ronghai Qu** (S'01-M'02-SM'05-F'18) was born in China. He received the B.E.E. and M.S.E.E. degrees from Tsinghua University, Beijing, China, in 1993 and 1996, respectively, and the Ph.D. degree from the University of Wisconsin Madison, Madison, WI, USA, in 2002, all in electrical engineering. In 1998, he joined the Wisconsin Electric Machines and Power Electronics Consortiums as Research Assistant. He became a Senior Electrical Engineer with Northland, a Scott Fetzer Company in 2002. Since 2003, he had been with the General Electric (GE) Global Research Center, Niskayuna, NY, as a Senior Electrical Engineer with the Electrical Machines and Drives Laboratory. He has authored over 120 published technical papers and is the holder of over 50 patents/patent applications. From 2010, he has been a professor with Huazhong University of Science &Technology, Wuhan, China. Prof. Qu is a full member of Sigma Xi. He has been the recipient of several awards from GE Global Research Center since 2003, including the Technical Achievement and Management Awards. He also is the recipient of the 2003 and 2005 Best Paper Awards, third prize, from the Electric Machines Committee of the IEEE Industry Applications Society at the 2002 and 2004 IAS Annual Meeting, respectively.



**Zirui Liu** was born in Anhui, China. He received the B.Eng. degree in Electrical Engineering and Automation from Hunan University, Hunan, China, in 2019. He is currently working toward the Ph.D. degree in Huazhong University of Science and Technology, Wuhan, China. His research interests include permanent magnet synchronous machines control and machine's parameters online identification.



**Lei Li** was born in Shandong, China. He received the B.Eng. degree in electrical engineering from China University of Mining and Technology, Xuzhou, China, in 2021. He is currently working toward the master's degree in electrical engineering at the Huazhong University of Science and Technology, Wuhan, China. His research interests include the design of permanent magnet machines and analysis of thermal.